Mineralium Deposita (2020) 55:1233–1246
https://doi.org/10.1007/s00126-019-00933-0

ARTICLE

Fluid mixing leads to main-stage cassiterite precipitation at the Xiling Sn polymetallic deposit, SE China: evidence from fluid inclusions and multiple stable isotopes (H–O–S)

Peng Liu[1] · Jingwen Mao[1,2] · Wei Jian[2] · Ryan Mathur[3]

Received: 28 July 2019 / Accepted: 1 November 2019 / Published online: 2 December 2019

Abstract

The Xiling Sn deposit in eastern Guangdong Province comprises the Fengdishan Sn and the Saozhoudi Sn–Pb–Zn ore blocks and has long been regarded as a volcanic–subvolcanic system related to Sn polymetallic mineralization. Here, we present fluid inclusion microthermometric data from different ore stages and H–O–S isotope data of hydrothermal minerals to constrain the genesis of the Xiling deposit. Fluid inclusions from stage I have T_h values from ~ 340 to 420 °C and salinities from ~ 15 to 17 wt% NaCl equivalent, while homogenization temperatures of fluid inclusions from stages II to V range from ~ 150 to 320 °C, and salinities range between ~ 1 and 6 wt% equivalent. The oxygen and hydrogen isotopic composition of quartz and cassiterite (δD_{fluid} − 65‰; $\delta^{18}O_{fluid}$ 3.6 to 6.3‰) suggest that the ore-forming fluids from stage I have a distinct magmatic signature, whereas those from stage II through stage IV (δD_{fluid} from − 80 to − 49‰; $\delta^{18}O_{fluid}$ from − 3.7 to 2.5‰) show characteristics of mixing between meteoric and magmatic fluids. Moreover, $\delta^{34}S$ values for sulfides from the Fengdishan ore block have a narrow range of 0.6 to 2.5‰ with a mean close to 0‰, consistent with a magmatic sulfur source. By contrast, $\delta^{34}S$ values for ore minerals from the Saozhoudi ore block range from 3.4 to 11.5‰, suggesting involvement of a sedimentary sulfur source. In addition, a previous geochronological study has shown that the volcanic–subvolcanic host rocks have an age of 160–170 Ma, while the Sn polymetallic mineralization has an age of about 145 Ma. Our data support a model of mixing of magmatic brine from a hidden granitic intrusion with meteoric water. The S isotope data and the observed temperature gradient of the fluid system suggest that the Sn mineralization is developed in the central part of the ore system, while the Sn–Pb–Zn and Pb–Zn mineralization occurs in the distal part. This finding might have important implications for exploration in the region.

Keywords Fluid inclusion · H · O · S isotopes · Fluid mixing · Xiling deposit · Southeastern Coastal Metallogenic Belt

Introduction

Globally, most Sn deposits are genetically related to granites (Lehmann 1990), whereas some Sn ore systems are associated with volcanic or subvolcanic rocks, such as in southern Bolivia, northwestern Mexico, and southwestern United States (Christiansen et al. 1983; Tuta et al. 1988; Cunningham et al. 1991). South China is one of the important W–Sn metallogenic provinces in the world, particularly the Nanling Range (e.g., Mao et al. 2013; Yuan et al. 2008, 2011, 2018, 2019; Hu et al. 2012; Qi et al. 2012), where W–Sn mineralization is genetically related to Mesozoic granitic rocks and mainly consists of skarn–, wolframite–quartz vein–, and minor greisen–types (Mao et al. 2007). It is worth noting that there are also several Sn ± Pb ± Zn ± Ag deposits associated with the volcanic–subvolcanic rocks in the southwestern part of the

---

Editorial handling: S.-Y. Jiang

Electronic supplementary material The online version of this article (https://doi.org/10.1007/s00126-019-00933-0) contains supplementary material, which is available to authorized users.

✉ Peng Liu
pengliu2018@chd.edu.cn

✉ Wei Jian
weijian851@gmail.com

[1] School of Earth Science and Resources, Chang'an University, Xi'an 710054, China

[2] Ministry of Natural Resources (MNR) Key Laboratory of Metallogeny and Mineral Assessment, Institute of Mineral Resources, Chinese Academy of Geological Sciences (CAGS), Beijing 100037, China

[3] Juniata College, Huntingdon, PA 16652, USA

Southeastern Coastal Metallogenic Belt (SCMB) (Huang and Qi 1991), which is adjacent to the Nanling Region in the north (Fig. 1). However, recent studies have recognized that these Sn polymetallic deposits are linked with granitic intrusions, including the Feie'shan W–Sn, the Jinkeng Sn, the Changpu Sn, and the Taoxihu Sn deposits (Liu et al. 2017, 2018c; Qiu et al. 2017; Yan et al. 2017, 2018). All these studies focus on the geochronology and petrogeochemistry of the W–Sn deposits, and indicate that they are genetically related to highly fractionated I– or A–type granitic intrusions (Liu et al. 2017, 2018c; Qiu et al. 2017; Yan et al. 2017). However, the origin and magmatic–hydrothermal evolution of these deposits have attracted much less attention, and little systematic studies on fluid dynamics exist.

The Xiling Sn polymetallic deposit is located in eastern Guangdong Province, within the southwestern domain of the SCMB, and comprises the Fengdishan and the Saozhoudi ore blocks. The deposit has long been regarded as volcanic or subvolcanic rock–related Sn mineralization (Chen et al. 1986; Huang and Qi 1991). However, our recent geochronological data yielded a muscovite ^{40}Ar-^{39}Ar plateau age of 140.6 ± 1.0 Ma and two cassiterite LA–ICP–MS U–Pb ages of 146.4 ± 1.0 Ma and 147.5 ± 1.1 Ma, and a zircon U–Pb age range from 161.5 ± 2.6 to 169.5 ± 0.5 Ma for volcanic–subvolcanic rocks at the Xiling deposit (Liu et al. 2018b). The ages of the volcanic–subvolcanic rocks predate the Xiling mineralization by ca. 15 to 20 m.y. There are no granitic rocks exposed in the mine area, but there is an outcrop of biotite granite about 12 km SE on which we obtained a zircon U–Pb age of 145.8 ± 0.6 Ma (Fig. 2a) (Liu et al. 2018b), suggesting a new genetic model for the Xiling mineral system.

Regional geological background

The South China Block is composed of two sub-blocks, the Yangtze Craton and the Cathaysia Block, which are separated by the Jiangshan–Shaoxing and Pingxiang–Yushan suture (e.g., Charvet et al. 1996; Zhao and Cawood 1999). The SCMB, located at the southeastern part of the Cathaysia Block, east to the Zhenghe–Dapu fault, covers the eastern Zhejiang, southeastern Fujian, and eastern Guangdong Provinces (Liu et al. 2018b) (Fig. 1a). The strata exposed include pre–Devonian metamorphic, Late Paleozoic–Middle Triassic clastic sedimentary and carbonate rocks, and Mesozoic–Cenozoic continental clastic and volcanic rocks (Shu et al. 2009). A NE–SW striking trans-lithospheric fault (Changle–Nan'ao fault) separates the SCMB into two tectonic belts from west to east: the volcanic–intrusive belt and the Pingtan–Dongshan metamorphic belt. The intrusive rocks in the region are mostly composed of high–K calc–alkaline I– and A–type granites, as well as minor syenite, quartz diorite, and gabbro (Xu et al. 2007). Previous studies have shown that three episodes of mineralization can be recognized in the SCMB:

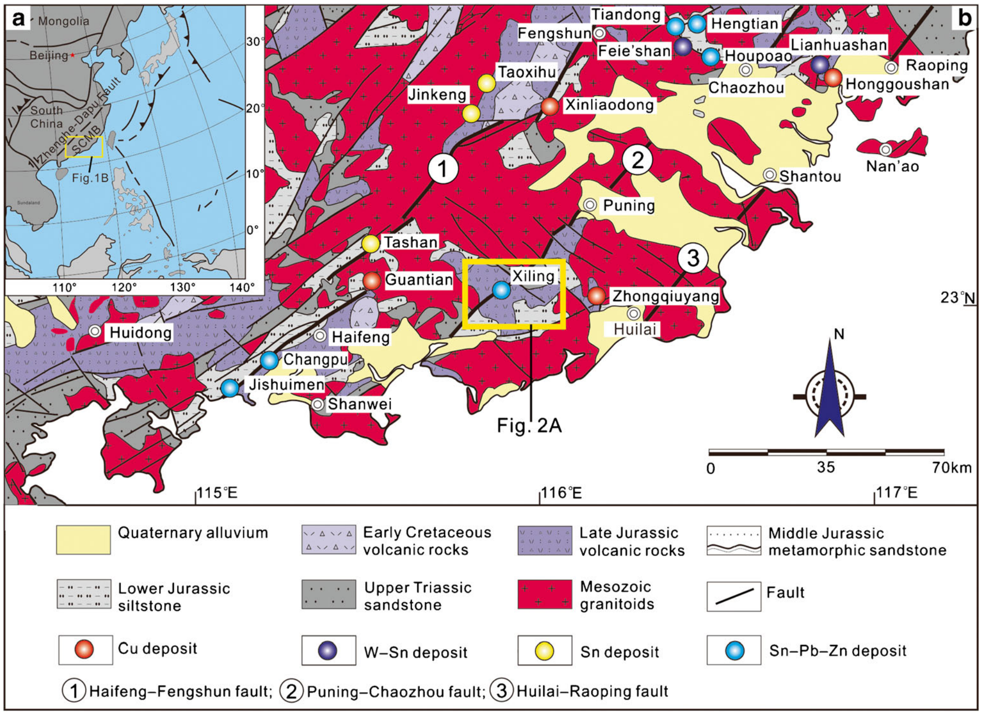

Fig. 1 **a.** Tectonic scheme of eastern Asia (after Gilder and Courtillot 1997). **b.** Geological map of the southwestern part of the Southeastern Coastal Metallogenic Belt (SCMB), showing the distribution of Mesozoic granitoids and polymetallic deposits (after Liu et al. 2017)

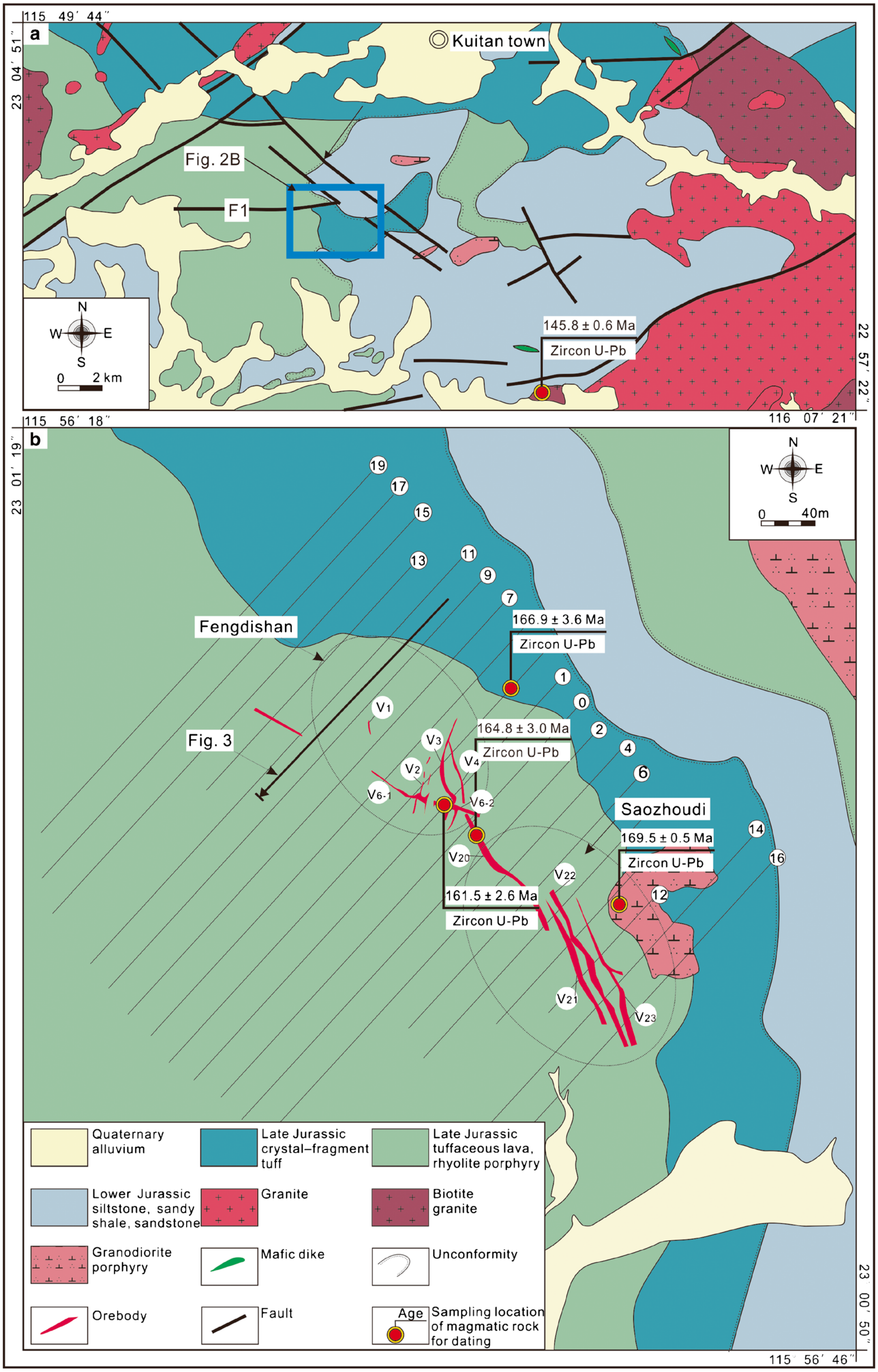

Fig. 2 **a.** Geological map of the Kuitan district showing the location of the Xiling deposit. **b.** Geological map of the Xiling deposit (Liu et al. 2018b). Ore bodies are projected to the surface

(1) the 170–160 Ma porphyry Cu–Au and Cu–Mo mineral systems distributed mainly in the southwestern part of the SCMB, such as in the eastern Guangdong and the coastal Fujian Provinces, (2) the 145–135 Ma W–Sn mineralization and related highly fractionated I– or A–type granites occurring mostly in eastern Guangdong Province, and (3) the 120–80 Ma porphyry–epithermal Cu–Au–Ag and porphyry Cu–Mo deposits in the coastal Fujian and Zhejiang Provinces (Liu et al. 2018c).

In eastern Guangdong along the southwestern domain of the SCMB, the major stratigraphic units include Upper Triassic and Early Jurassic clastic sedimentary rocks, Late Jurassic to Early Cretaceous volcanic rocks, and Quaternary alluvial sediments (Fig. 1b). The tectonic framework is mainly controlled by the NE–SW–striking Lianhuashan fault zone, which is composed of three main faults: Haifeng–Fengshun, Puning–Chaozhou, and Huilai–Raoping fault (Xu et al. 2000) (Fig. 1b). Recent studies have recognized a phase of W–Sn polymetallic mineralization linked with granitic intrusions in the region that formed between 145 and 135 Ma (Liu et al., 2017, 2018a, b; Qiu et al. 2017; Yan et al. 2017). Liu et al. (2018c) described three prominent characteristics of the granites associated with the W–Sn mineralization in the SCMB: (1) high–K calc–alkaline, weakly peraluminous and I– or A–type affinity, (2) high degree of fractionation characterized by high Si, K, F, Na, Rb, Cs, Th, and U, and low Mg, Fe, Ca, Ba, Sr, Ti, and P, with high Rb/Sr and Rb/Ba ratios, and (3) $\varepsilon_{Hf}(t)$ values plotting above the evolutionary trend defined by the Cathaysia basement rocks, indicating a magma source from remelting of Cathaysia basement rocks with contributions of mantle-derived components.

Geology of the Xiling Sn deposit

The Xiling deposit, located about 7 km southwest of Kuitan town in Huilai County in eastern Guangdong Province (Fig. 2a), was discovered in the 1940s, with underground mining in progress since the 1950s. The proven metal reserves include 15,000 t Sn with an ore grade of 2.41% Sn, and minor Pb and Zn (Huang and Qi 1991). The strata exposed in the area consist of the Lower Jurassic Jinji Formation and the Upper Jurassic Gaojiping Formation (Fig. 2b). The Jinji Formation occurs in the eastern part of the mine area and includes siltstone, sandstone, and sandy shale. The Gaojiping Formation in the central and western parts of the mine area is composed of crystal–fragment tuff (ESM Fig. 1A, B), tuffaceous lava (ESM Fig. 1C, D), and rhyolite porphyry (ESM Fig. 1). The exposed intrusive rocks are mainly composed of biotite granite, granite, and granodiorite porphyry (Liu et al. 2018b).

The Xiling Sn mineralization is predominantly hosted in the rhyolite porphyry, tuffaceous lava, and crystal–fragment tuff (Fig. 3), and the Pb–Zn mineralization is locally developed within sandy shale. Ten orebodies have been explored in the Xiling deposit and range from 110 to − 10 m in altitude. The Fengdishan ore block consists of six Sn orebodies. Orebodies V_3 and V_4 are the major Sn orebodies, with an average Sn grade of 2.73% and 0.58%, respectively. Orebody V_3 varies in thickness from 0.95 to 4.50 m (average 2.17 m), with a strike length of about 180 m. Orebody V_4 varies in thickness from 0.20 to 2.05 m (average 0.48 m) and continues along strike for about 135 m, with pinch and swell domains and branches. The Saozhoudi ore block consists of four Sn–Pb–Zn orebodies with V_{22} and V_{20} as the major Sn–Pb–Zn ones. V_{20} is the largest Sn–Pb–Zn orebody ranging from 90 to − 10 m in altitude, and varies in thickness from 1.5 to 8.6 m (average 5.69 m), with Sn grade of 2.99%, and a strike length of about 115 m. Orebody V_{22} ranges from 70 to − 10 m in altitude and continues along strike for about 108 m, with an average thickness of 4.95 m and an average Sn grade of 1.36%.

Types and characters of ores

There are four ore types recognized in the Xiling deposit: (1) veins of cassiterite–feldspar–quartz, (2) disseminated ores, (3) veins of cassiterite–quartz (muscovite), and (4) veins of cassiterite–sulfide. The major orebodies occur as veins of cassiterite–feldspar–quartz, cassiterite–quartz (muscovite), and/or cassiterite–sulfide, whereas the disseminated mineralization is minor. Type 1 mineralization occurs in the central part of the Fengdishan ore block. Here, the orebodies are mostly hosted by rhyolite porphyry. The ore mineral is cassiterite, while the gangue minerals are albite and K–feldspar, with minor quartz and calcite (Figs. 4a and 5a). Type 2 mineralization is developed in the lower part of the Fengdishan ore block, and hosted by rhyolite porphyry. Ore minerals are mainly composed of cassiterite and minor arsenopyrite, while the gangue minerals are quartz and minor muscovite (Figs. 4b and 5b). Type 3 mineralization is hosted by the upper part of the Fengdishan ore block. Here, the orebodies are mostly hosted by tuffaceous lava, and more locally rhyolite porphyry and crystal–fragment tuff. Ore minerals comprise of cassiterite, and minor chalcopyrite and pyrrhotite, while the gangue minerals are dominated by quartz + muscovite ± sericite ± chlorite. Cassiterite, chalcopyrite, and pyrrhotite are euhedral to subhedral (2–10 mm) in the quartz veins, while muscovite, and minor sericite and chlorite occur as anhedral fine grains in

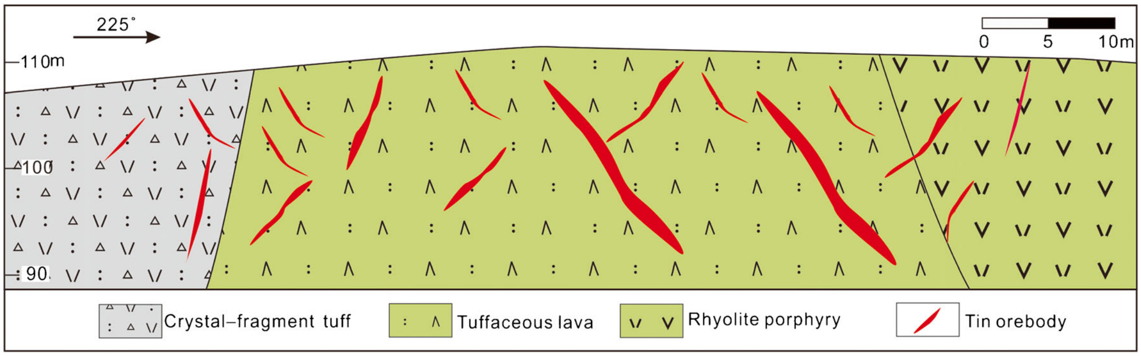

Fig. 3 Geological cross section between the Fengdishan exploration lines No. 9 and No. 11 (Liu et al. 2018b)

the quartz veins (Figs. 4c, d and 5c). Type 4 mineralization is predominantly developed in the tuffaceous lava and altered sandy shale of the Saozhoudi ore block with minor occurrences in the upper part of the Fengdishan ore block. Ore minerals include galena, sphalerite, pyrite, and minor cassiterite and pyrrhotite, and the gangue minerals are quartz, muscovite, sericite, chlorite, and calcite (Figs. 4e, f and 5d, e).

Hydrothermal alteration and mineralization

Ore–related hydrothermal alteration at the Xiling deposit is weak and includes silicification, muscovitization, sericitization, chloritization, carbonatization, and epidotization. Silicification is developed and is represented as disseminations in all four ore types. Muscovite occurs as disseminated and on veinlets in the wall–rock, or as aggregates in cassiterite–quartz–muscovite veins, showing a close association with the Sn mineralization (Fig. 5f). Chlorite and sericite predominantly occur as clusters in sulfide–quartz–chlorite veins, and are spatially related to Pb and Zn mineralization (Fig. 5g–i).

Based on field and petrographic observations, five hydrothermal stages were identified. From early to late, these are cassiterite–feldspar–quartz (stage I), cassiterite–quartz–muscovite (stage II), sulfide–cassiterite (stage III), quartz–

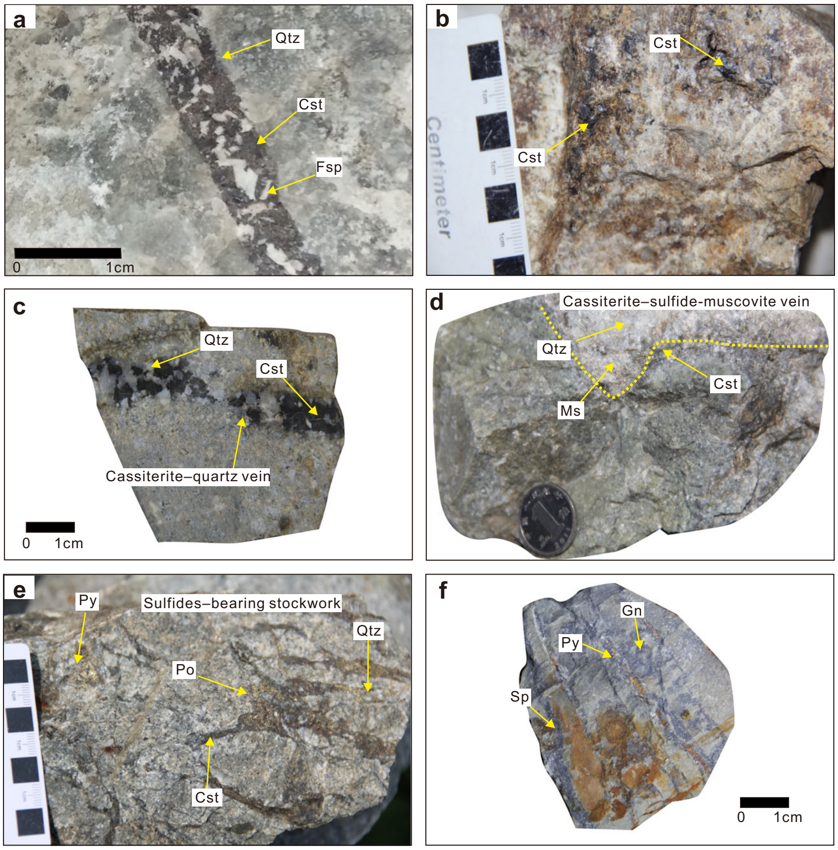

Fig. 4 Photographs of the ores of the Xiling deposit. **a** Cassiterite–feldspar–quartz vein ore. **b** Disseminated ore. **c** Cassiterite–quartz vein ore. **d** Cassiterite–sulfide–muscovite–vein ore. **e** Sulfides–bearing stockwork ore. **f** Sphalerite–galena–vein ore. Chl chlorite, Cst cassiterite, Gn galena, Ms muscovite, Po pyrrhotite, Py pyrite, Qtz quartz, Sp sphalerite

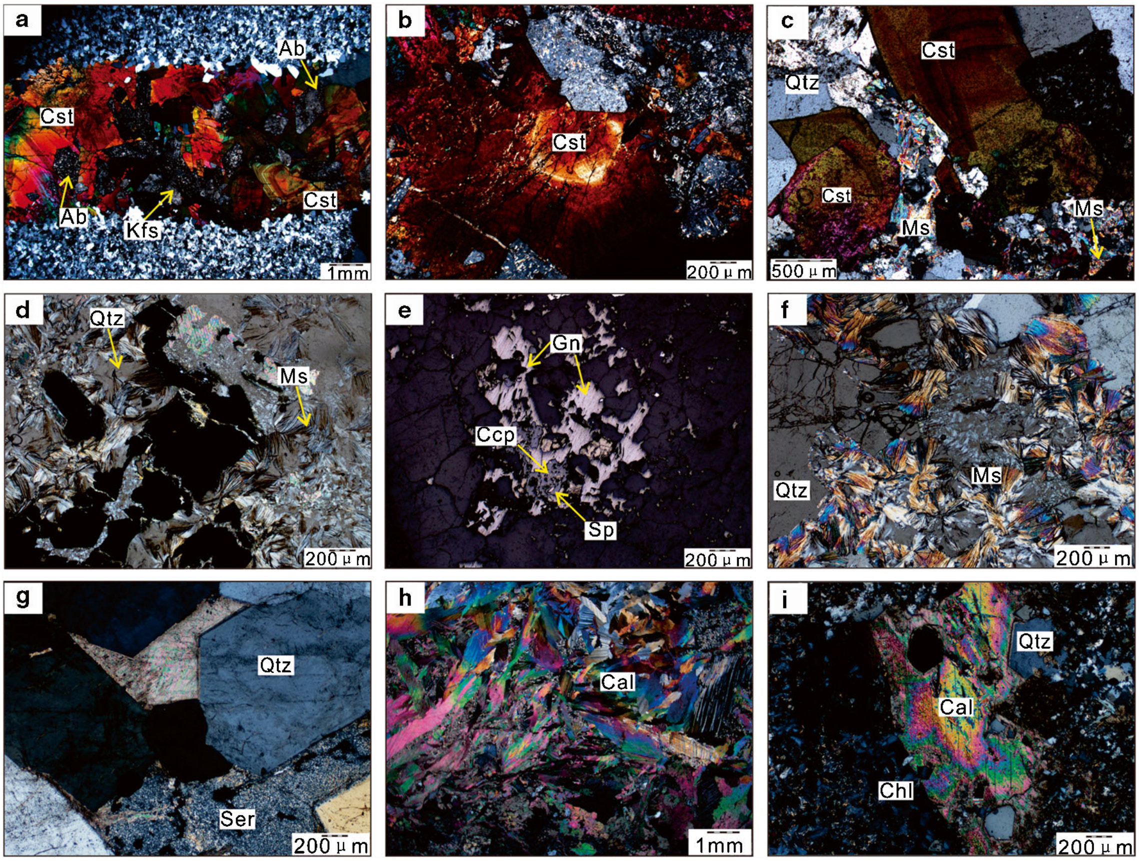

Fig. 5 Photomicrographs of the ores and hydrothermal alteration of the Xiling deposit (under crossed polarized light). **a** Cassiterite–feldspar–quartz vein ore. **b** Disseminated ore. **c** Cassiterite–muscovite–quartz vein ore. **d** Cassiterite–sulfide–muscovite–vein ore. **e** Cassiterite–sulfide–vein ore. **f** Silicification and muscovitization. **g** Sericitization and carbonatization. **h** Carbonatization. **i** Chloritization and carbonatization. Ab Albite, Cal calcite, Ccp chalcopyrite, Chl chlorite, Cst cassiterite, Gn galena, Ms muscovite, Kfs K–feldspar, Qtz quartz, Ser sericite, Sp sphalerite

sulfide–chlorite (stage IV), and calcite–chlorite–quartz (stage V) (Fig. 6). Stage I is characterized by cassiterite, albite, K–feldspar, and minor quartz and calcite forming veins. Stage II is the major Sn deposition stage. Ore minerals include cassiterite, and minor arsenopyrite, pyrrhotite, and chalcopyrite. Stage III is the major Pb and Zn deposition stage with minor Sn and is characterized by cassiterite, pyrrhotite, pyrite, galena, sphalerite, and minor chalcopyrite forming veins,

Fig. 6 Paragenetic sequence of mineralization and alteration of the Xiling deposit (Liu et al. 2018b)

Ore-forming stages	Stage Ⅰ Cassiterite–feldspar–quartz	Stage Ⅱ Cassiterite–quartz–muscovite	Stage Ⅲ Sulfide–cassiterite	Stage Ⅳ Quartz–sulfide–chlorite	Stage Ⅴ Calcite–chlorite–quartz
Cassiterite	■■■■■	■■■■■	■■■	■■	
Arsenopyrite		■■	■■		
Galena			■■■■	■■■■	
Sphalerite			■■■■	■■■■	
Chalcopyrite		■	■■		
Pyrrhotite		■	■■	■	
Pyrite			■■■	■■■	■
Quartz	■■■	■■■■	■■■	■■■	■■■
Muscovite		■■■	■■■	■	
Sericite		■■	■■	■■■	■
Feldspar	■■■■				
Chlorite		■	■■	■■■	■■■
Epidote					■■
Calcite	■■				■■■

Note:■■■■■–dominant;■■■■–major;■■■–intermediate;■■–minor;■–very minor;blank–absent veinlets, or grained in the muscovite–quartz veins. Stage IV is the major Pb and Zn deposition stage and is characterized by galena, sphalerite, and pyrite forming veins or veinlets. Finally, stage V is the latest hydrothermal and mostly barren stage characterized by the deposition of calcite, chlorite, and quartz.

Samples and analytical methods

Fluid inclusions

Cassiterite, quartz, and calcite samples for fluid inclusion microanalyses in this study span all ore-forming stages. More than 30 polished thick sections were examined under the microscope, of which 10 polished thin sections were selected for microthermometric measurements. Microthermometric measurements were carried out at the MNR Key Laboratory of Metallogeny and Mineral Assessment, Institute of Mineral Resources, Chinese Academy of Geological Sciences. Fluid inclusion microthermometric data were obtained using a Linkam THMSG–600 heating–freezing stage, coupled to a Leica microscope. This stage enables measurements to be taken within the range − 196 to 600 °C. Freezing and heating runs were undertaken using liquid nitrogen and a thermal resistor, respectively. The estimated accuracy of temperatures is ± 0.5 °C for temperatures below 100 °C, ± 1.0 °C for temperatures in the range between 100 and 600 °C. Heating/cooling rates were restricted to < 10 °C/min, and were reduced to 1 to 0.1 °C/min near phase transformations.

Oxygen and hydrogen isotopes

Hydrogen and oxygen isotope analyses for quartz and cassiterite samples covering the main ore-forming stages were done using a MAT253EM mass spectrometer at the Isotopic Laboratory of the Institute of Mineral Resources, Chinese Academy of Geological Sciences. Prior to analysis, samples were separated using standard magnetic separation and handpicking techniques before extracting water from 40 to 80 mg of mineral separate. Oxygen isotope analyses for quartz and cassiterite were performed using the BrF_5 technique of Clayton and Mayede (1963). For hydrogen isotope analyses of fluid inclusion water, quartz samples were outgassed at 105 °C for 12 h, and then fluid inclusions were decrepitated by heating to 500 to 600 °C. Water released by the fluid inclusions was converted to hydrogen gas using the zinc reduction method of Coleman et al. (1982). All $\delta^{18}O$ and δD values reported here are in ‰ relative to Standard Mean Ocean Water (SMOW). The analytical uncertainty is ± 0.2‰ for oxygen and ± 2‰ for hydrogen.

Sulfur isotopes

In situ LA–MC–ICP–MS sulfur isotope analyses were conducted on sulfide minerals from five polished thin sections covering different mineralization stages. Laser sampling was performed by a RESOlution–M 50 excimer ArF laser ablation system, while sulfur isotope ratios were analyzed with a Nu Plasma 1700 MC–ICP–MS at the State Key Laboratory of Continental Dynamics, Northwest University in Xi'an, China. All analyses were made using a 30-μm laser beam with a repetition rate of 2–3 Hz and an ablation time of 50 s. Detailed analytical conditions and procedures can be found in Chen et al. (2017).

Results

Fluid inclusions

Representative samples of cassiterite, quartz, and calcite were selected for fluid inclusion microthermometric studies. Microscopic examination of the samples show that the type of fluid inclusions present in the samples is relatively simple, i.e., two-phase aqueous fluid inclusions. Microthermometric measurements of fluid inclusions were done if the fluid inclusion assemblages (FIA) are trapped along growth bands (Goldstein and Reynolds 1994). Features and microthermometric results for fluid inclusions from the different ore-forming stages are shown in Supplementary Table A1 and described below.

Cassiterite–feldspar–quartz (stage I) Fluid inclusions from stage I mineralization have been studied in cassiterite and quartz; they typically comprise a liquid H_2O phase and a vapor H_2O phase at room temperature (ESM Fig. 2A, B). Fluid inclusions in cassiterite vary from 4 to 10 μm in size and show rounded or irregular shapes, with their vapor bubbles occupying less than 30 vol%. Their ice-melting temperatures ($T_{\text{m–ice}}$) range from − 11.0 to − 12.8 °C, corresponding to salinities of 15.0–16.7 wt% NaCl equivalent, and homogenize into the liquid phase between 352 and 417 °C, with a peak between 350 and 380 °C. Fluid inclusions in quartz are 5 to 15 μm in diameter and vary from rounded to highly irregular in shape, with vapor bubbles occupying 20 to 30 vol%. Their ice-melting temperatures ($T_{\text{m–ice}}$) range from − 10.9 to − 12.8 °C, yielding salinities of 14.9–16.7 wt% NaCl equiv, while homogenization temperatures range from 336 to 373 °C (Fig. 7a, b).

Cassiterite–quartz–muscovite (stage II) Fluid inclusions from this stage have been measured in cassiterite and quartz, and they typically consist of liquid and vapor at room temperature (ESM Fig. 2C). Fluid inclusions in

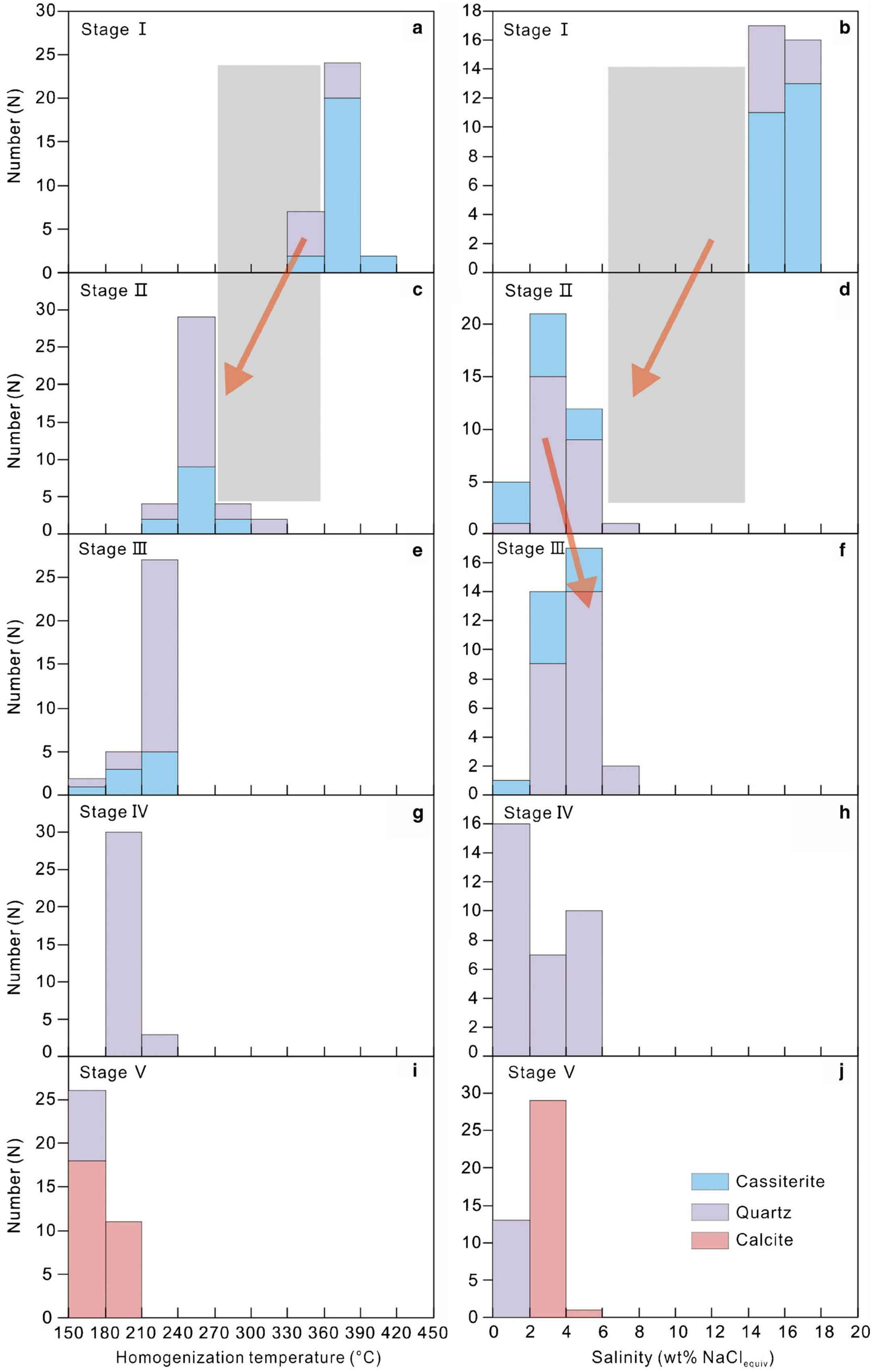

Fig. 7 Frequency histograms of microthermometric data for fluid inclusion from each ore-forming stage of the Xiling deposit

quartz show rounded or irregular shapes with their size varying from 4 to 16 μm, and their vapor bubbles occupying < 40 vol%. The fluid inclusions have ice-melting temperatures (T_{m-ice}) ranging from − 0.9 to − 3.8 °C, equivalent to salinities of 1.6–6.2 wt% NaCl equivalent, respectively, and homogenize between 231 and 312 °C, with a peak between 250 and 280 °C. Fluid inclusions in cassiterite are 3 to 10 μm in diameter, and their vapor bubbles occupy less than 30 vol%. The ice-melting temperatures (T_{m-ice}) range from − 0.7 to − 2.8 °C, corresponding to salinities of 1.2–4.6 wt% NaCl equivalent, respectively, with total homogenization temperatures varying from 227 to 289 °C (Fig. 7c, d).

Sulfide–cassiterite (stage III) Fluid inclusions in cassiterite and quartz from stage III typically consist of a liquid H_2O phase and a vapor H_2O phase at room temperature (ESM Fig. 2D). Fluid inclusions in cassiterite have sizes varying from 3 to 9 μm, show rounded or irregular shapes, and their vapor bubbles occupy < 40 vol%. They have ice-melting temperatures (T_{m-ice}) ranging between − 0.7 and − 3.3 °C, equivalent to salinities of 1.2–5.4 wt% NaCl equivalent, respectively, and homogenize between 170 and 227 °C. Fluid inclusions in quartz are 5 to 18 μm in diameter with their shapes varying from rounded to highly irregular and vapor bubbles occupy between 30 and 40 vol% of the inclusions. Their ice-melting temperatures (T_{m-ice}) are between − 1.9 and − 4.2 °C, corresponding to salinities of 3.2–6.7 wt% NaCl equivalent, respectively. Homogenization temperatures vary from 178 to 237 °C, with a peak between 210 and 237 °C (Fig. 7e, f).

Quartz–sulfide–chlorite (stage IV) Fluid inclusions in quartz from this stage typically comprise liquid and vapor phases at room temperature (ESM Fig. 2E). These fluid inclusions have sizes ranging from 10 to 34 μm, and have rounded or rectangular shapes, and vapor bubbles occupying < 30 vol%. Their ice-melting temperatures (T_{m-ice}) range from − 0.4 to − 3.2 °C, yielding salinities of 0.7–5.3 wt% NaCl equivalent, with homogenization temperatures varying from 180 to 218 °C (Fig. 7g, h).

Calcite–chlorite–quartz (stage V) Fluid inclusions in calcite and quartz from stage V typically comprise liquid and vapor phases at room temperature (ESM Fig. 2F). Fluid inclusions in calcite have sizes varying from 5 to 9 μm. Their ice-melting temperatures (T_{m-ice}) range from − 1.5 to − 2.6 °C, corresponding to salinities of 2.6 to 4.3 wt% NaCl equivalent, with homogenization temperatures ranging from 167 to 205 °C with a peak between 160 and 190 °C. Fluid inclusions in quartz are 5 to 15 μm in diameter and they vary in shape from rounded to highly irregular, with vapor bubbles occupying < 20 vol%. They have ice-melting temperatures (T_{m-ice}) ranging from − 0.7 to − 1 °C, equivalent to salinities of 1.2–1.7 wt% NaCl equivalent. Homogenization temperatures are between 156 and 168 °C (Fig. 7i, j).

Hydrogen and oxygen isotopes

The hydrogen and oxygen isotopic compositions of selected minerals (i.e., quartz and cassiterite) from the four ore-forming STAGES I–IV are given in Supplementary Table A2. The oxygen isotopic compositions of ore-forming fluids ($\delta^{18}O_{fluid}$) have been calculated using the temperatures obtained by microthermometry of fluid inclusions of each ore-forming stage (i.e., stage I, 365 °C; stage II, 258 °C; stage III, 216 °C; stage IV, 195 °C), and the oxygen isotopic fractionation equation of the quartz–water system (Fekete et al. 2017) and cassiterite–water system (Zheng 1991), respectively. In stage I, the δD_{fluid} value for quartz is − 65‰, while $\delta^{18}O_{fluid}$ values range from 3.6 to 6.3‰ (6.3‰ for quartz and 3.6 to 4.7‰ for cassiterite). For stage II, δD_{fluid} values for quartz range from − 80 to − 55‰, while $\delta^{18}O_{fluid}$ values range from − 0.5 to 2.5‰ (− 0.5 to 0.4‰ for quartz and 2.5‰ for cassiterite). In stage III, δD_{fluid} values for quartz range from − 63 to − 49‰, while $\delta^{18}O_{fluid}$ values range from − 2.0 to − 1.3‰. Finally, for stage IV, the δD_{fluid} value is − 73‰ and the $\delta^{18}O_{fluid}$ value is − 3.7‰ for quartz.

Sulfur isotope composition of sulfides

Isotopic compositions for sulfides from the Fengdishan and Saozhoudi ore blocks are given in Supplementary Table A3. $\delta^{34}S$ values at Fengdishan range from 0.6 to 2.5‰ and include values for chalcopyrite (0.6 to 2.1‰; n = 9, average = 1.4‰), arsenopyrite (1.4 to 2.1‰; n = 5, average = 1.6‰), and pyrite (1.3 to 2.5‰; n = 2, average = 1.4‰). At the Saozhoudi ore block, $\delta^{34}S$ values range from 3.4 to 11.5‰ and were obtained from pyrite (4.9 to 11.5‰; n = 10, average = 7.3‰) and galena (3.4 to 4.0‰; n = 5, average = 3.6‰).

Discussion

Fluid evolution

The fluids from stages I and II represent the main stage for Sn deposition, while those from stages III and IV represent the Sn–Pb–Zn and Pb–Zn deposition stages. Fluid inclusions in stage I have the highest homogenization temperatures between 336 and 417 °C and the highest salinities of 14.9 to 16.7 wt% NaCl equiv. By contrast, homogenization temperatures and salinities of fluid inclusions from stage II are

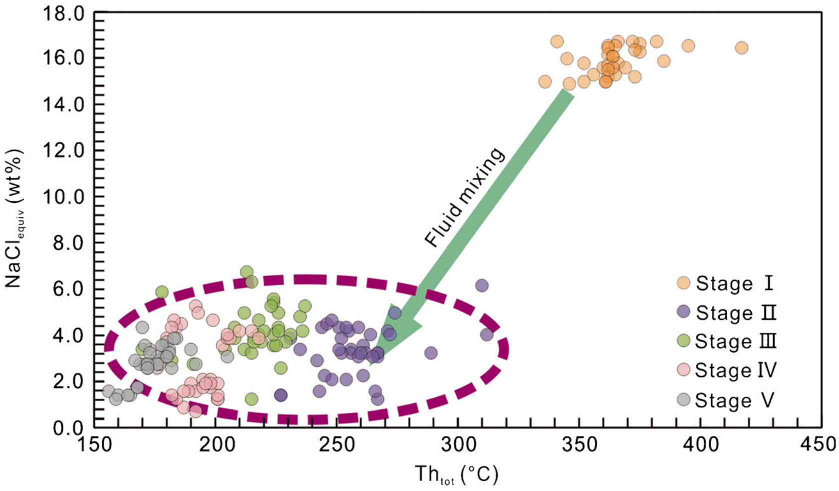

Fig. 8 Plot of salinity versus homogenization temperature for fluid inclusions from different mineral assemblage stages of the Xiling deposit

noteably less, with homogenization temperatures between 227 to 312 °C and salinities of 1.2 to 6.2 wt% (Fig. 7c, d). In addition, there is a trend of progressive decrease in homogenization temperatures of fluid inclusions from stages II to V (i.e., the major Sn, Sn–Pb–Zn, and Pb–Zn deposition stages) (Figs. 7 and 8). By contrast, salinities for stages II to V cover the same general range, from ~ 6 wt% NaCl equiv. to ~ 1 wt% NaCl equiv. (Fig. 8).

Oxygen and hydrogen isotopes show that the cassiterite–feldspar–quartz assemblage (stage I) has $\delta^{18}O_{fluid}$

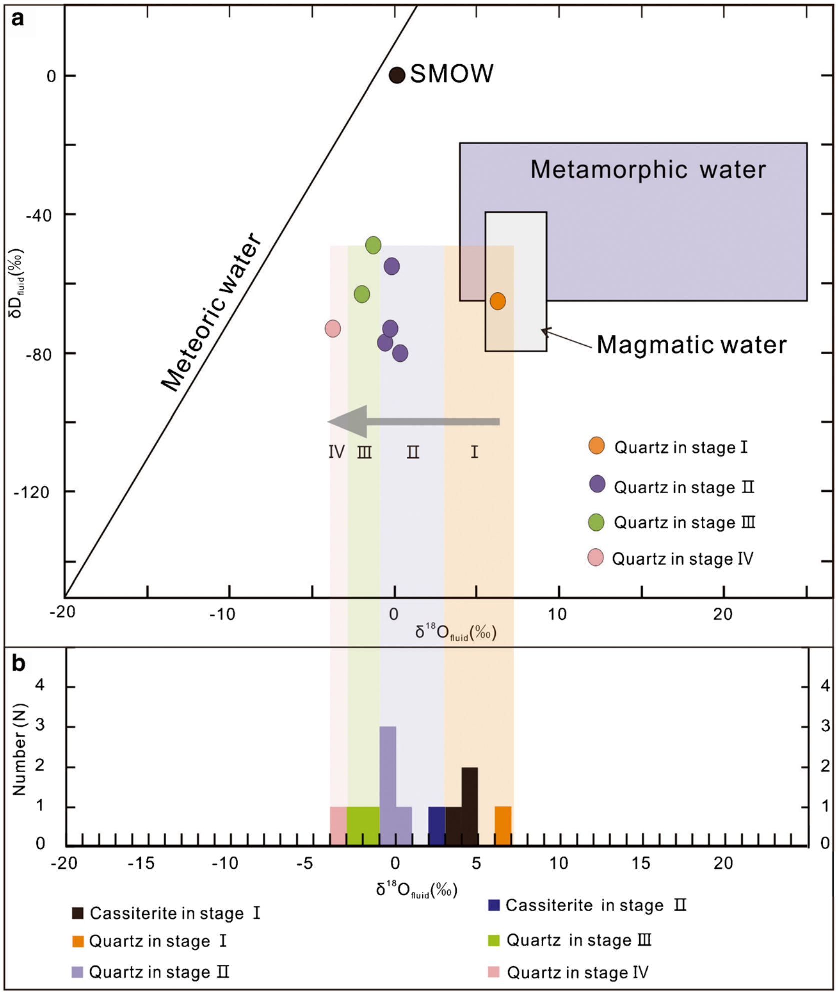

Fig. 9 **a.** Plot of $\delta^{18}O$ versus δD, showing the calculated composition for the ore-forming fluids of the Xiling deposit. The metamorphic water field, primary magmatic water field, and meteoric water line are from Taylor (1974). SMOW Standard Mean Ocean Water. **b.** $\delta^{18}O_{fluid}$ isotopic composition of cassiterite and quartz of the Xiling deposit

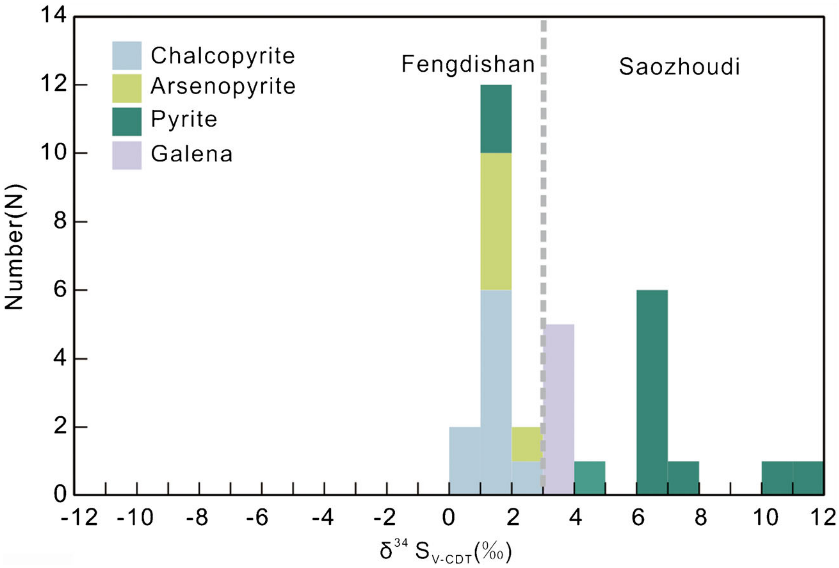

Fig. 10 Histogram of $\delta^{34}S$ values for sulfide minerals from the Xiling deposit

values of 1.8 to 6.3‰ and δD_{fluid} values of − 65‰, consistent with magmatic–hydrothermal fluids. By contrast, $\delta^{18}O_{fluid}$ and δD_{fluid} values for the cassiterite–quartz–muscovite assemblage (stage II) range from − 0.5 to 2.5‰ and − 80 to − 55‰, respectively, suggesting that meteoric water mixed with the initial magmatic brines (Fig. 9a). Moreover, there is a clear trend that increasing amounts of meteoric water mixed with the magmatic brines from stages II through IV (Fig. 9a). Fluid inclusion salinities are relatively uniform between stages II and V. Fluid inclusion salinities increase slightly between stages II and III, suggesting that multiple pulses of brine with high salinities mixed with meteoric water during ore formation.

Recent geochronological data on the Xiling deposit are consistent with our interpretation. The two cassiterite samples used for U–Pb dating were taken from the disseminated and cassiterite–quartz vein ores, while the Ar–Ar muscovite sample was taken from the cassiterite–sulfide–vein ore, which is predominantly composed of galena, sphalerite, pyrite, and minor cassiterite. In combination with the different paragenetic minerals and the apparent age gap of at least 4 myrs between the cassiterite U–Pb and muscovite $^{40}Ar–^{39}Ar$ plateau ages, all the observations above show that the Xiling mineralization is likely related to multiple magmatic brine fluid pulses. In summary, the ore-forming fluids from stage I would appear to have a distinctly magmatic signature, whereas those from the major Sn (stage II), Sn–Pb–Zn (stage III), and Pb–Zn (stage IV) depositional stages show evidence of mixing between meteoric and magmatic–hydrothermal fluids, with possibly multiple magmatic fluid pulses involved (Fig. 9b).

Ore precipitation

Several mechanisms for Sn ore precipitation have been proposed, including fluid–rock interaction (Korges et al. 2017), mixing of hot magmatic brine with cooler meteoric water (Witt 1988; Heinrich 1990; Audétat et al. 1998),

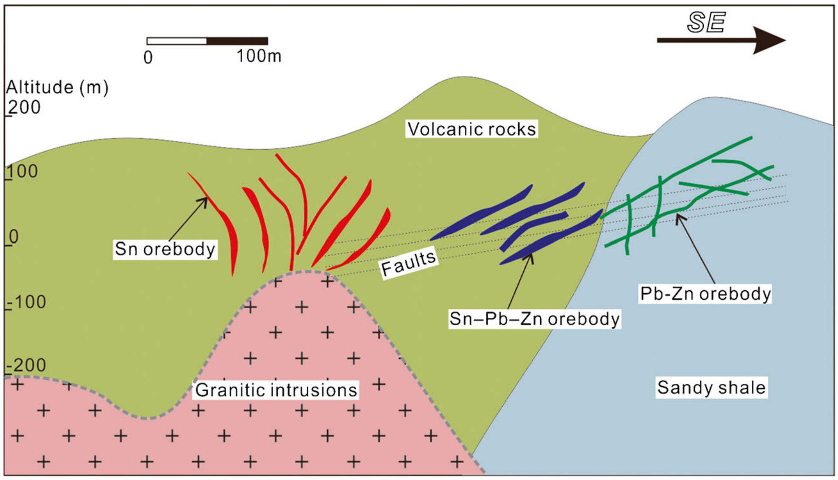

Fig. 11 A proposed model explaining the formation of the Xiling Sn polymetallic deposit (modified after Liu et al. 2018b)

and phase separation (Drummond and Ohmoto 1985; Polya 1989). At the Xiling Sn deposit, there is no indication of co-existence of low-salinity vapor fluid inclusions with high-salinity fluid inclusions, indicating that phase separation is not responsible for ore deposition. Moreover, fluid inclusion homogenization temperatures and salinities do not show a progressive decrease but a rapid decrease during the major Sn depositional stage (i.e., stage I and stage II), inconsistent with fluid–rock interactions, which generally produce widely a strong alteration, whereas the Xiling deposit has weak wall–rock alteration (Liu et al., 2018b). For the case of Xiling, a dramatic decrease in homogenization temperatures and salinities of fluid inclusions is consistent with mixing between hot magmatic brine and cool meteoric water. Additionally, hydrogen and oxygen isotopic data also show that there is a progressive ingress of meteoric water involved in the ore-forming fluids from the early to late ore-forming stages.

Tin is transported as chloride complexes in hydrothermal fluids, either as Sn^{2+} (Eugster 1986; Wilson and Eugster 1990) or Sn^{4+} (Schmidt 2018). Hence, SnO_2 can be precipitated through a decrease in the Cl^- concentration of the hydrothermal system. The drastic change in salinity from 16 to 2–4 wt% NaCl equiv., combined with a temperature drop from about 350 to about 250 °C, is best explained by mixing of a hot (magmatic) brine with cooler meteoric water.

Source of sulfur

$\delta^{34}S$ values for both the Fengdishan and Saozhoudi ore blocks relate to sulfides only and, as no sulfate minerals are present, the sulfur species in the hydrothermal fluids are probably dominated by H_2S rather than SO_4^{2-}. Hence, the sulfur isotopic compositions of sulfides are likely to represent those of the bulk sulfur in the hydrothermal system (Ohmoto and Rye 1979). $\delta^{34}S$ values for sulfides in the Fengdishan ore block have a narrow range from 0.6 to 2.5‰, with a mean close to 0‰, consistent with a possible magmatic sulfur source (Fig. 10) (Ohmoto and Rye 1979; Chaussidon and Lorand 1990). The sulfur isotopic compositions are similar to those of granite-related Sn deposits in eastern Guangdong Province, such as the Taoxihu Sn ($\delta^{34}S$ values for pyrite and chalcopyrite ranging between 0.1 and 2.1‰) (Yan et al. 2017) and Sanjiaowo Sn deposits ($\delta^{34}S$ values for pyrite and pyrrhotite ranging between − 1.6 and 1.0‰) (Yan et al. 2018).

By contrast, $\delta^{34}S$ values for sulfides from the Saozhoudi ore block range from 3.4 to 11.5‰, and are distinctly different from the Fengdishan ore block (Fig. 10). Higher $\delta^{34}S$ values can be explained by a reduction in f_{O2}, or the incorporation of some sedimentary sulfur through the interaction with sedimentary rocks (Ohmoto 1972). Moreover, sedimentay rocks commonly have a wide range of $\delta^{34}S$ values (Hoefs 2009). This can explain the large variation of $\delta^{34}S$ values seen in sulfides of the Saozhoudi ore block. Finally, the Saozhoudi ore block is at the distal end of the Xiling ore system (Liu et al., 2018b). As a result, we propose that the source of sulfur at the Saozhoudi ore block is dominantly sedimentary sulfur.

Conclusions

Fluid inclusion homogenization temperatures and salinities show a dramatic decrease between stages I and II of the Xiling Sn deposit. Homogenization temperatures for fluid inclusions from stages II to V then show a progressive decrease, whereas the salinities are relatively uniform, even increasing slightly between stages II and III. Oxygen and hydrogen isotopes show that ore-forming fluids from stage I have a distinctly magmatic signature, whereas those from stages II to IV have characteristics of mixing between meteoric water and magmatic fluids. The results obtained in this study suggest that the ore-forming mechanism of the Xiling deposit is predominantly mixing of magmatic brine from a hidden granitic intrusion with meteoric water. In combination with S isotopes, all these observations likely suggest that Sn mineralization developed in the central part of the ore system, while the Sn–Pb–Zn and Pb–Zn orebodies occur in the distal part (Fig. 11), respectively. This finding has important implications for the exploration strategy in the region.

Acknowledgments We thank the editors Shaoyong Jiang and Bernd Lehmann and two anonymous reviewers for their constructive comments and suggestions. We also would like to thank Cornel E.J. de Ronde for improvements on the early manuscript. We appreciate the help from Huishou Ye and Zengjie Zhang for their technical assistance with the fluid inclusion, oxygen and hydrogen isotope analyses. We are also grateful to Xutao Chen, Shaobin Li, and Xiaojian Zeng from No. 2 Party of the Geology Bureau for Guangdong Province, for their assistance during field work.

Funding information This research was jointly funded by the National Key R&D Plan (Grant No.2017YFC0601403), National Natural Science Foundation of China Projects (41902072, 41820104010), Fundamental Research Funds for the Central Universities (300102279301, 300102279401), Fundamental Research Funds for the Central Institutions (JYYWF20180601), and MNR Key Laboratory of Metallogeny and Mineral Assessment open Foundation (ZS1903).

References

Audétat A, Günther D, Heinrich CA (1998) Formation of a magmatic hydrothermal ore deposit: insights with LA–ICP–MS analysis of fluid inclusion. Science 279:2091–2094

Charvet J, Shu LS, Shi YS, Guo LZ, Faure M (1996) The building of South China: collision of Yangzi and Cathaysia blocks, problems and tentative answers. J Asian Earth Sci 13:223–235

Chaussidon M, Lorand JP (1990) Sulphur isotope composition of orogenic spinel lherzolite massifs from Ariège (North–Eastern Pyrenees, France): an ion microprobe study. Geochim Cosmochim Acta 54:2835–2846

Chen L, Chen KY, Bao ZA, Liang P, Sun TT, Yuan HL (2017) Preparation of standards for in situ sulfur isotope measurement in sulfides using femtosecond laser ablation MC–ICP–MS. J Anal At Spectrom 32:107–116

Chen XH, Hu XZ, Cong XD (1986) Genesis and mineralization of subgranitic porphyry, Xiling tin deposit, Guangdong. Geochimica 1:50–57 (in Chinese with English abstract)

Christiansen EH, Burt DM, Sheridan MF, Wilson RT (1983) The petrogenesis of topaz rhyolites from the western United States. Contrib Mineral Petrol 83:16–30

Clayton RN, Mayeda TL (1963) The use of bromine pentafluoride in the extraction of oxygen from oxides and silicates for isotopic analysis. Geochim Cosmochim Acta 27:43–52

Coleman ML, Sheppard TJ, Durham JJ, Rouse JE, Moore GR (1982) Reduction of water with zinc for hydrogen isotope analysis. Anal Chemi 54:993–995

Cunningham CC, McNamee J, Vásquez JP, Erichsen GE (1991) A model of volcanic dome-hosted precious metal deposit in Bolivia. Econ Geol 86:415–421

Drummond SE, Ohmoto H (1985) Chemical evolution and mineral deposition in boiling hydrothermal systems. Econ Geol 80:126–147

Eugster HP (1986) Minerals in hot water. Am Mineral 71:655–673

Fekete S, Weis P, Thomas P, Driesner T, Bouvier AS, Baumgartner L, Heinrich C (2017) Contrasting hydrological processes of meteoric water incursion during magmatic–hydrothermal ore deposition: an oxygen isotope study by ion microprobe. Earth Planet Sci Lett 451: 263–271

Gilder S, Courtillot V (1997) Timing of the North–South China collision from new middle to late Mesozoic paleomagnetic data from the North China Blocks. J Geophys Res 102:713–727

Goldstein RH, Reynolds TJ (1994) Systematics of fluid inclusions in diagenetic minerals: Society of Sedimentary Geology. SEPM Short Course 31:1–199

Heinrich CA (1990) The chemistry of hydrothermal tin (tungsten) ore deposition. Econ Geol 85:457–481

Hoefs J (2009) Stable isotope geochemistry, 6th edn. Springer Verlag Berlin, Heidelberg

Hu RZ, Wei WF, Bi XW, Peng JT, Qi YQ, Wu LY, Chen YW (2012) Molybdenite Re–Os and muscovite ^{40}Ar/^{39}Ar dating of the Xihuashan tungsten deposit, central Nanling district, South China. Lithos 150:111–118

Huang B, Qi JZ (1991) A special type of tin deposit, east Guangdong. Bull Nanjing Inst Geol MR Chinese Acad Geol Sci 12:67–75 (in Chinese with English abstract)

Korges M, Weis P, Lüders V, Laurent O (2017) Depressurization and boiling of a single magmatic fluid as a mechanism for tin–tungsten deposit formation. Geology 46:75–78

Lehmann B (1990) Metallogeny of tin. Springer, Berlin

Liu P, Mao JW, Cheng YB, Yao W, Wang XY, Hao D (2017) An Early Cretaceous W–Sn deposit and its implications in southeast coastal metallogenic belt: constraints from U–Pb, Re–Os, Ar–Ar geochronology at the Feie' shan W–Sn deposit, SE China. Ore Geol Rev 81:112–122

Liu P, Mao JW, Pirajno F, Jia LH, Zhang F, Li Y (2018a) Ore genesis and geodynamic setting of the Lianhuashan porphyry tungsten deposit, eastern Guangdong Province, SE China: constraints from muscovite ^{40}Ar–^{39}Ar and zircon U–Pb dating and Hf isotopes. Mineral Deposita 53:797–814

Liu P, Mao JW, Santosh M, Xu LG, Zhang RQ, Jia LH (2018b) The Xiling Sn deposit, eastern Guangdong Province, Southeast China: a new genetic model from ^{40}Ar/^{39}Ar muscovite and U–Pb cassiterite and zircon geochronology. Econ Geol 113:511–530

Liu P, Mao JW, Santosh M, Bao ZA, Zeng XJ, Jia LH (2018c) Geochronology and petrogenesis of the Early Cretaceous A–type granite from the Feie'shan W–Sn deposit in the eastern Guangdong Province, SE China: implications for W–Sn mineralization and geodynamic setting. Lithos 300–301:330–347

Mao JW, Xie GQ, Guo CL (2007) Large–scale tungsten mineralization in the Nanling region, South China: metallogenic ages and corresponding geodynamic processes. Acta Petrol Sin 23:2329–2338 (in Chinese with English abstract)

Mao JW, Cheng YB, Chen MH, Pirajno F (2013) Major types and time–space distribution of Mesozoic ore deposits in South China and their geodynamic settings. Mineral Deposita 48:267–294

Ohmoto H (1972) Systematics of sulfur and carbon isotopes in hydrothermal ore deposits. Econ Geol 67:551–578

Ohmoto H, Rye RO (1979) Isotopes of sulfur and carbon. In: Barnes HL (ed) Geochemistry of hydrothermal ore deposits, 2nd edn. John Wily and Sons, New York, pp 509–567

Polya DA (1989) Chemistry of the main–stage ore–forming fluids of the Panasqueira W–Cu (Ag)–Sn deposit, Portugal: implications for models of ore genesis. Econ Geol 84:1134–1152

Qi HW, Hu RZ, Wang XF, Qu WJ, Bi XW, Peng JT (2012) Molybdenite Re–Os and muscovite ^{40}Ar–^{39}Ar dating of quartz vein–type W–Sn polymetallic deposits in Northern Guangdong, South China. Mineral Deposita 47:607–622

Qiu ZW, Yan QH, Li SS, Wang H, Tong LX, Zhang RQ, Wei XP, Li P, Wang LM, Bu A, Yan LM (2017) Highly fractionated Early Cretaceous I–type granites and related Sn polymetallic mineralization in the Jinkeng deposit, eastern Guangdong, SE China: Constraints from geochronology, geochemistry, and Hf isotopes. Ore Geol Rev 88:718–738

Schmidt C (2018) Formation of hydrothermal tin deposits: Raman spectroscopic evidence for an important role of aqueous Sn(IV) species. Geochim Cosmochim Acta 220:499–511

Shu LS, Zhou XM, Deng P, Wang B, Jiang SY, Yu JH, Zhao XX (2009) Mesozoic tectonic evolution of the Southeast China Block: new insights from basin analysis. J Asian Earth Sci 34:376–391

Taylor HP (1974) The application of oxygen and hydrogen isotope studies to problems of hydrothermal alteration and ore deposition. Econ Geol 69:843–883

Tuta ZH, Sutter JF, Kesler SE, Ruiz J (1988) Geochronology of mercury, tin, and fluorine mineralization in Northern Mexico. Econ Geol 83: 1931–1942

Wilson GA, Eugster HP (1990) Cassiterite solubility and tin speciation in supercritical chloride solutions. Geochem Soc Special Publ 2:179–195

Xu XC, Xie QQ, Yue SC (2000) Metallogenetic mechanism of Mesozoic metallic ore deposits in Eastern Guangdong area. Journal of Hefei University of Technology 23:99–103 (in Chinese with English abstract)

Xu XS, O'Reilly SY, Griffin WL, Wang XL, Pearson NJ, He ZY (2007) The crust of Cathaysia: age, assembly and reworking of two terranes. Precambrian Res 158:51–78

Yan QH, Li SS, Qiu ZW, Wang H, Wei XP, Li P, Dong R, Zhang XY (2017) Geochronology, geochemistry and Sr–Nd–Hf–S–Pb isotopes of the Early Cretaceous Taoxihu Sn deposit and related granitoids, SE China. Ore Geol Rev 89:350–368

Yan QH, Wang H, Qiu ZW, Wei XP, Li P, Dong R, Zhang XY, Zhou KL (2018) Origin of Early Cretaceous A–type granite and related Sn mineralization in the Sanjiaowo deposit, eastern Guangdong, SE China and its tectonic implication. Ore Geol Rev 93:60–80

Yuan SD, Peng JT, Hu RZ, Li HM, Shen NP, Zhang DL (2008) A precise U–Pb age of cassiterite from the Xianghualing tin–polymetallic deposit (Hunan, South China). Mineral Deposita 43:375–382

Yuan SD, Peng JT, Hao S, Li HM, Geng JZ, Zhang DL (2011) In–situ LA–MC–ICP–MS and ID–TIMS U–Pb geochronology of cassiterite in the giant Furong tin deposit, Hunan province, South China: new constraints on the timing of tin–polymetallic mineralization. Ore Geol Rev 43:235–242

Yuan SD, Williams-Jones AE, Mao JW, Zhao PL, Yan C, Zhang DL (2018) The origin of the Zhangjialong tungsten deposit, South China: implications for W-Sn mineralization in large granite batholiths. Econ Geol 113:1193–1208

Yuan SD, Williams-Jones AE, Romer RL, Zhao PL, Mao JW (2019) Protolith–related thermal controls on the decoupling of Sn and W in Sn–W metallogenic provinces: insights from the Nanling Region, China. Econ Geol 114:1005–1012

Zhao GC, Cawood PA (1999) Tectonothermal evolution of the Mayuan assemblage in the Cathaysia Block: new evidence for Neoproterozoic collisional–related assembly of the South China craton. Am J Sci 299:309–339

Zheng YF (1991) Calculation of oxygen isotope fractionation in metal oxides. Geochim Cosmochim Acta 55:2299–2307